CFD-DEM investigation of viscous solid-liquid mixing: impact of particle properties and mixer characteristics

Bruno Blais[a], François Bertrand[a,*]

[a] *Research Unit for Industrial Flow Processes (URPEI), Department of Chemical Engineering, École Polytechnique de Montréal, P.O. Box 6079, Stn Centre-Ville, Montréal,QC, Canada, H3C 3A7*

Abstract

In chemical engineering, numerous processes require the suspension of particles in a laminar or transitional regime. For such operations, predicting the fraction of suspended particles as well as their distribution and homogeneity is a major concern. In this work, the unresolved CFD-DEM model introduced by our group for solid-liquid mixing is used to investigate the mixing dynamics of viscous suspensions. The techniques chosen to characterize the degree of suspension, the homogeneity and the distribution of the particles are presented. They are used to assess the efficiency of a pitched blade turbine with a clearance of $C = T/4$. The impact of solid properties on mixing dynamics is investigated by varying the Young's modulus, the coefficient of restitution and the sliding friction coefficient in the DEM model. Lastly, five alternative configurations

*Corresponding author
Email address: francois.bertrand@polymtl.ca (François Bertrand)

of the mixing rig are investigated by varying the clearance of the impeller and introducing baffles.
Keywords: multiphase flows; solid-liquid mixing; computational fluid dynamics; discrete element method; CFD-DEM

1. Introduction

Solid-liquid mixing in mechanically agitated vessels is a widely used process in a multitude of industries, including ore processing, pharmaceuticals and cosmetics. Although it has been the subject of numerous investigations since the pioneering work of Kneule [1] and Zwietering [2], it remains an active field of research in which many questions remain unanswered. This is, at least in part, due to the complex multi-scale solid-liquid physics of particle-particle and particle-fluid interactions and the variety of flow regimes and unsteady flow structures in agitated vessels. Most studies on solid-liquid mixing have focused on the assessment of the minimum agitation speed (or just-suspended speed N_{js}) required to suspend the particles in the turbulent regime. The resulting correlations, such as the one proposed by Zwietering [2], perform poorly in the laminar and transitional operation regimes [3, 4, 5]. We recently showed that the underlying hydrodynamics involved in the suspension of non-dilute suspensions are different in the transitional regime than in the turbulent regime [3]. We

took measurements using the pressure gauge technique (PGT) in an unbaffled stirred tank equipped with a pitched blade turbine and found that the dependence on the just-suspended speed of fluid viscosity μ and particle diameter d_p were the opposite of what was predicted by the Zwietering correlation [2] and other correlations, including those proposed by Nienow [6], Baldi [7], Rao *et al.* [8], Takashi *et al.* [9], Armenante *et al.* [10], and Grenville *et al.* [11]. This is not surprising given that these correlations were derived for the turbulent regime. However, our results with respect to the influence of viscosity on N_{js} showed that increasing μ decreases N_{js}, which is in agreement with recent work by Tamburini *et al.* [12], who investigated the impact of viscosity on N_{js} for a wide range of viscosities using an unbaffled stirred tank with a covered top.

Predicting N_{js} is insufficient for some operations such as chemical reactors with a solid catalyst, for food processing, and for crystallization processes. In these cases, it is important that the concentration of particles be homogeneous throughout the tank, which generally requires that the operating speed exceeds N_{js}. However, little is known about the distribution and dispersion of particles in the laminar and transitional regimes. This lack of information on local concentrations of particles is mostly due to the difficulties in measuring this quantity. While optical, sampling, radioactive, and conductivity based meth-

ods exist to measure local concentrations of particles (see reviews by Kasat and Pandit [13] and Tamburini *et al.* [14]), their accuracy is limited and, more importantly, they cannot measure the velocity field and the particle concentration throughout the entire vessel. The cloud height, for which Bittorf and Kresta introduced a predictive model based on wall jets in the turbulent regime [15], is an interesting concept, but is not a measure of the distribution of the particles and gives no insights into the possible presence of dead zones.

Multiphase computational fluid dynamics (CFD) is a powerful and versatile tool that overcomes the experimental issues mentioned above. We introduced an unresolved CFD-DEM model [16] within the CFDEM framework [17, 18] that combines Open∇FOAM for the CFD [19] and LIGGGHTS [20, 21] for the DEM. The underlying finite volume scheme was first verified using the method of manufactured solutions [22, 23, 24, 25, 26] and combined with a new semi-implicit immersed boundary method that we devised and validated in the context of mixing [27]. The immersed boundary technique, which was integrated into our CFD-DEM scheme, was used to study the fraction of suspended particles in an unbaffled stirred tank equipped with a PBT with clearance of $C = \frac{T}{4}$. A very good agreement was obtained for both the particle flow patterns and the fraction of suspended particles as measured by the PGT. During this investigation,

we noted that for $N > N_{js}$, the concentration of particles in a conical zone below the impeller remains considerably higher than in the rest of the tank. However, since our aim was to validate the unresolved CFD-DEM model, we did not extend our analysis to studying the dynamics of the mixing, distribution and dispersion of the particles in the tank or the role of solid properties or solid-fluid forces. Our analysis was also limited to a single clearance. The goal of the present work is to shed light on these issues.

First, we describe in detail the unresolved CFD-DEM model. We present various techniques used to investigate the degree of suspension and the global mixing of particles, and discuss their capacities. Notably, we revisit the mixing index first introduced by Doucet *et al.* [28] and discuss some of its limitations. We then perform a thorough analysis using various mixing metrics, and we investigate the role of the Saffman lift force and the physical properties of the particles to gain insight into the suspension mechanism in the tank. Lastly, we discuss the impact of the impeller clearance and the presence of baffles. The information obtained from these simulations is used to propose guidelines for the design of mixing processes operating in the laminar and transitional regimes.

2. Model Formulation

The CFD-DEM approach combines the resolution of the fluid at a coarser scale than that of the particles by using the volume averaged Navier-Stokes (VANS) equations and the discrete element method (DEM) for the solid particles. The two schemes are coupled at regular intervals. The constitutive equations of the models are presented briefly, and we refer to our earlier work [16, 27] for a full description of the unresolved CFD-DEM scheme and the immersed boundary method used to model the rotating impeller.

2.1. Governing equations for the solid-phase (DEM)

In soft-sphere DEM, the governing equations for the translation ($\boldsymbol{v}_i$) and rotational ($\boldsymbol{\omega}_i$) motion of particle i are [20, 29, 30]:

$$m_i \frac{d\boldsymbol{u}_i}{dt} = \sum_j (\boldsymbol{f}_{c,ij}) + \sum_k \boldsymbol{f}_{lr,ik} + \boldsymbol{f}_{pf,i} + \boldsymbol{f}_{g,i} \tag{1}$$

$$I_i \frac{d\boldsymbol{\omega}_{p,i}}{dt} = \sum_j (\boldsymbol{M}_{t,ij} + \boldsymbol{M}_{r,ij}) \tag{2}$$

where m_i is the mass of particle i, I_i is the moment of inertia of particle i, $\boldsymbol{f}_{c,ij}$ is the contact force between particles i and j, $\boldsymbol{f}_{lr,ik}$ is the sum of the non-contact (long-range) forces between particles i and k, $\boldsymbol{f}_{pf,i}$ is the sum of the particle-fluid interaction forces, $\boldsymbol{f}_{g,i}$ is a body force (*i.e.* gravity), and $\boldsymbol{M}_{t,ij}$

and $\boldsymbol{M}_{r,ij}$ are the tangential and rolling friction torques acting on the particles. Since large particles are considered in the present work, non-contact forces are ignored. The expression for the particle-fluid interaction forces (drag, lift, etc.) are discussed in Section 2.3.

The contact forces between two particles are split into normal ($\boldsymbol{f}_{cn,ij}$) and tangential ($\boldsymbol{f}_{ct,ij}$) [29] components:

$$\boldsymbol{f}_{c,ij} = \boldsymbol{f}_{cn,ij} + \boldsymbol{f}_{ct,ij} = -k_{n,ij}\boldsymbol{\delta}_{n,ij} - \gamma_{n,ij}\dot{\boldsymbol{\delta}}_{n,ij} - k_{t,ij}\boldsymbol{\delta}_{t,ij} - \gamma_{t,ij}\dot{\boldsymbol{\delta}}_{t,ij} \qquad (3)$$

where $k_{n,ij}$ and $k_{t,ij}$ are the normal and tangential stiffnesses, $\gamma_{n,ij}$ and $\gamma_{t,ij}$ are the normal and tangential damping coefficients, $\boldsymbol{\delta}_{n,ij}$ and $\boldsymbol{\delta}_{t,ij}$ are the normal and tangential overlaps, and $\dot{\boldsymbol{\delta}}_{n,ij}$ and $\dot{\boldsymbol{\delta}}_{t,ij}$ their derivatives with respect to time.

In the present work, the model proposed by Tsuji [31] for the normal force is combined with the Mindlin model for the tangential force [32, 33]. This is done in order to relate the stiffness and the damping coefficients to the Young's modulus of the material (Y), the Poisson ratio (ν) and the coefficient of restitution (e_r) using the equations in Table 1. The tangential overlap $\boldsymbol{\delta}_{t,ij}$ is truncated by Coulomb's law to ensure that $\boldsymbol{f}_{ct,ij} \leq -\mu_{s,ij}\,|\boldsymbol{f}_{cn,ij}|\,\frac{\boldsymbol{\delta}_{t,ij}}{|\boldsymbol{\delta}_{t,ij}|}$.

Table 1: Equations for the DEM model

Parameter	Equation
Normal stiffness	$k_{n,ij} = \frac{4}{3} Y^*_{ij} \sqrt{R^*_{ij} \delta_{n,ij}}$
Tangential stiffness	$k_{t,ij} = 8 G^*_{ij} \sqrt{R^*_{ij} \delta_{n,ij}}$
Normal damping	$\gamma_{n,ij} = -2\sqrt{\frac{5}{6}} \frac{\ln(e_r)}{\sqrt{\ln^2(e_r)+\pi^2}} \sqrt{\frac{2}{3} k_n m^*_{ij}}$
Tangential damping	$\gamma_{t,ij} = -2\sqrt{\frac{5}{6}} \frac{\ln(e_r)}{\sqrt{\ln^2(e_r)+\pi^2}} \sqrt{k_t m^*_{ij}}$
Coulomb limit for the tangential force	$\boldsymbol{f}_{ct,ij} \leq -\mu_{s,ij} \left\lvert \boldsymbol{f}_{cn,ij} \right\rvert \frac{\boldsymbol{\delta}_{t,ij}}{\lvert \boldsymbol{\delta}_{t,ij} \rvert}$
Tangential torque	$\boldsymbol{M}_{t,ij} = \boldsymbol{r}_i \times (\boldsymbol{f}_{ct,ij})$
Rolling friction torque	$\boldsymbol{M}_{r,ij} = -\mu_{r,ij} \left\lvert \boldsymbol{f}_{cn,ij} \right\rvert \frac{\boldsymbol{\omega}_{p,ij}}{\lvert \boldsymbol{\omega}_{p,ij} \rvert} R^*_{ij}$
Equivalent mass	$\frac{1}{m^*_{ij}} = \frac{1}{m_i} + \frac{1}{m_j}$
Equivalent radius	$\frac{1}{R^*_{ij}} = \frac{1}{R_i} + \frac{1}{R_j}$
Equivalent Young's modulus	$\frac{1}{Y^*_{ij}} = \frac{\left(1-\nu_i^2\right)}{Y_i} + \frac{\left(1-\nu_j^2\right)}{Y_j}$
Equivalent shear modulus	$\frac{1}{G^*_{ij}} = \frac{2(2+\nu_i)(1-\nu_i)}{Y_i} + \frac{2(2+\nu_j)(1-\nu_j)}{Y_j}$
Sliding friction coefficient	$\mu_{s,ij}$
Rolling friction coefficient	$\mu_{r,ij}$
Distance to the contact point for particle i	$\boldsymbol{r}_i$
Radius of particle i	R_i

2.2. Governing equations for the liquid-phase flow (CFD)

Form A of the incompressible volume-averaged Navier-Stokes (VANS) equations is solved for the liquid phase [34] and is given by:

$$\frac{\partial \epsilon_f}{\partial t} + \nabla \cdot (\epsilon_f \boldsymbol{u}) = 0 \tag{4}$$

$$\frac{\partial (\rho_f \epsilon_f \boldsymbol{u})}{\partial t} + \nabla \cdot (\rho_f \epsilon_f \boldsymbol{u} \otimes \boldsymbol{u}) = -\epsilon_f \nabla p + \nabla \cdot \boldsymbol{\tau} - \boldsymbol{F}_{pf} \tag{5}$$

where ϵ_f is the void fraction, ρ_f is the density of the fluid, p is the pressure, and $\boldsymbol{u}$ is the velocity of the fluid. The viscous stress tensor $\boldsymbol{\tau}$ is defined as:

$$\boldsymbol{\tau} = \epsilon_f \mu \left((\nabla \boldsymbol{u}) + (\nabla \boldsymbol{u})^T - \frac{2}{3} (\nabla \cdot \boldsymbol{u}) \boldsymbol{\delta}_k \right) \tag{6}$$

where μ is the dynamic viscosity and $\boldsymbol{\delta}_k$ is the identity tensor.

The momentum exchange term from the particles to the fluid $\boldsymbol{F}_{pf}$ is defined as:

$$\boldsymbol{F}_{pf} = \frac{1}{\Delta V} \sum_{i}^{n_p} \boldsymbol{f}_{pf,i} - \boldsymbol{f}_{\nabla p,i} - \boldsymbol{f}_{\nabla \cdot \boldsymbol{\tau},i} - \boldsymbol{f}_{\mathrm{Ar},i} \tag{7}$$

$$\boldsymbol{f}_{pf,i} = \boldsymbol{f}_{d,i} + \boldsymbol{f}_{\nabla p,i} + \boldsymbol{f}_{\nabla \cdot \boldsymbol{\tau},i} + \boldsymbol{f}_{\mathrm{Ar},i} + \boldsymbol{f}_{\mathrm{vm},i} + \boldsymbol{f}_{B,i} + \boldsymbol{f}_{\mathrm{Saff},i} + \boldsymbol{f}_{\mathrm{Mag},i} \tag{8}$$

where n_p is the number of particles and $\boldsymbol{f}_{pf,i}$ is the sum of all the fluid-solid interaction forces involving particle i: drag ($\boldsymbol{f}_{d,i}$), pressure gradient force ($\boldsymbol{f}_{\nabla p,i}$), viscous force ($\boldsymbol{f}_{\nabla \cdot \boldsymbol{\tau},i}$), Archimedes force ($\boldsymbol{f}_{\mathrm{Ar},i}$), virtual mass force ($\boldsymbol{f}_{\mathrm{vm},i}$), Basset force ($\boldsymbol{f}_{B,i}$), Saffman lift force ($\boldsymbol{f}_{\mathrm{Saff},i}$) and Magnus lift force ($\boldsymbol{f}_{\mathrm{Mag},i}$). The

pressure, viscous and Archimedes forces are removed from $\boldsymbol{F}_{pf}$ since they are included directly in the continuous expression of form A of the VANS equations.

These equations are solved using a pressure implicit with splitting of operators (PISO) scheme [35] that we extended for the VANS equation and that we verified using the method of manufactured solutions [22]. The PISO-IB method, a semi-implicit immersed boundary method developed earlier by our group [27], is used to take the rotating impeller into account. This method integrates a forcing term directly into the momentum equation of VANS equations within the semi-implicit PISO scheme that imposes the velocity of the rigid body.

2.3. Governing equations for the solid-liquid coupling

The expressions for drag, pressure, viscous stress, and the Saffman lift forces are given in Table 2.

The virtual mass, Basset, and Magnus lift forces are not taken into account due to the low particle relaxation time caused by the high viscosity of the fluid considered.

Table 2: Expressions for the solid-liquid forces

Force	Equation
Pressure gradient - $\boldsymbol{f}_{\nabla p,i}$ [29]	$-V_p \nabla p$
Viscous force - $\boldsymbol{f}_{\nabla \cdot \boldsymbol{\tau},i}$ [29]	$-V_p \nabla \cdot \boldsymbol{\tau}$
Rong drag model -$\boldsymbol{f}_{d,i}$ [36]	$\frac{\pi}{8} C_D d_p^2 \rho_f \left\|\boldsymbol{u}-\boldsymbol{v}_i\right\| \left(\boldsymbol{u}-\boldsymbol{v}_i\right) \epsilon_f^{2-\beta(\epsilon_f, Re_p)}$ with $C_D = \left(0.63 + \frac{4.8}{\sqrt{Re_p}}\right)^2$ $\beta\left(\epsilon_f, Re_p\right) = 2.65\left(\epsilon_f + 1\right) - \left(5.3 - 3.5\epsilon_f\right)\epsilon_f^2 e^{-\frac{\left(1.5-\log {Re_p}^2\right)}{2}}$ and $Re_p = \frac{\rho_f d_p \left\|\boldsymbol{u}-\boldsymbol{v}\right\|}{\mu}$
Saffman lift - $\boldsymbol{f}_{\mathrm{Saff},i}$ McLaughlin model [37]	$J^* 1.614 \rho_f^{\frac{1}{2}} \mu_f^{\frac{1}{2}} \left(\boldsymbol{u}-\boldsymbol{v}_i\right) \times \frac{\boldsymbol{w}}{\left\|\boldsymbol{w}\right\|^{\frac{1}{2}}}$ with $J^* = 1 - \frac{0.287\left(\left\|\boldsymbol{u}-\boldsymbol{v}_i\right\|^2\right)}{\left\|\boldsymbol{w}\right\|}$ and $\boldsymbol{w} = \nabla \times \boldsymbol{u}$

3. Evaluation of the quality of the mixing and the fraction of suspended solids

Mixing is an intuitive concept related to the reduction of the inhomogeneities of a quantity (in the case of solid-liquid mixing, the concentration or volume fraction of particles) both globally and locally. However, no unique mathematical definition of it has been proposed, despite the large body of work discussing this issue, such as the book by Ottino for laminar mixing [38].

Euler-Lagrange models, such as the unresolved CFD-DEM, suffer from the generation of a considerable amount of data (*i.e.* the position and the velocity of all particles at all desired times) that is hard to post-process efficiently.

While visually appealing, animating the motion of the particles does not give quantitative information on the state of the mixing. A quantitative assessment of the quality of the mixing simulated by Euler-Lagrange simulations requires strategies to extract the essential information from the particle positions.

In this section, we present various approaches for measuring both the degree of homogeneity (or mixing) of the particles as well as the fraction of suspended particles (X_{susp}). We discuss their limitations and strengths, but we do not distinguish between the dispersion and distribution of the particles. This is not an exhaustive presentation and not all the methods are reviewed.

3.1. Measuring the homogeneity and the overall mixing efficiency

3.1.1. Void fraction analysis

An intuitive way to evaluate the distribution of the particles is to project their volume onto the Eulerian CFD mesh. This is already inherent to the unresolved CFD-DEM model since the void fraction (ϵ_f) is part of the VANS equations. The same projection can be also used on the velocity (translation or rotational) of the particles to extract a cell-averaged particle velocity.

The Eulerian cell-averaged representation of the Lagrangian data can be used to obtain statistical information on the distribution of the particles, including

histograms of the void fraction. This information can also be used to establish the steady-state concentration profiles using phase averaging.

3.1.2. Mixing index

Doucet *et al.* (2008) introduced a metric (the so-called weak sense mixing index) to measure the efficiency of mixing in granular and fluid flow systems from Lagrangian trajectories [28]. Their method consists of using principal component analysis (PCA) to measure the correlation between the positions of the particles ($\boldsymbol{x} \in \mathbb{R}^d$, where d is dimensionality of the domain) at time t ($\boldsymbol{x}_t$) and their initial position ($\boldsymbol{x}_0$). If the PCA analysis results in asymptotically vanishing eigenvalues, the system is deemed mixed in the weak sense. Concretely, this means that no component (direction in $\mathbb{R}^d$) can be identified, which explains most of the motion of the particles. In the case of non-vanishing eigenvalues, the vector corresponding to the highest eigenvalue can be used to extract the direction of poorer mixing, thus allowing the investigator to isolate bottlenecks more efficiently. Doucet *et al.* (2008) showed that this approach can be used to provide an accurate measure of the degree of mixing for granular systems in a cylindrical drum and in a V-blender as well as that of viscous mixing in a Kenics static mixer.

Furthermore, this metric can be augmented by including additional information ($\boldsymbol{\zeta}$), such as the size of the particles, to constitute an augmented initial state vector ($\boldsymbol{\chi}_0^T = [\boldsymbol{x}_0^T, \boldsymbol{\zeta}_0^T]$) on which the PCA can be carried out. Doucet *et al.* (2008) used this so-called strong sense mixing index to measure the mixing efficiency of a cylindrical drum in the case of bidispersed particles and showed that the segregation phenomena, which plague these types of mixers, can be identified using this metric, whereas they are not detected using the weak sense mixing index. The same method was used by Bouffard *et al.* [39] to study the mixing of bidispersed solid particles in a spheronizer. In this case, the strong mixing index was used to determine the impact of the angular velocity of the bottom plate of the spheronizer on the segregation of the two sizes of particles.

To remain concise, we refer the reader to the tutorial of Shlens for the theoretical background on PCA [40]. PCA has limitations [40], which are not discussed in [28] or [39], but which must be taken into account when using such mixing indices. While the discussion that follows is centered on the weak sense mixing index, the conclusions derived apply in a straightforward way to the strong sense mixing index.

Let f be a function related to a process (*i.e.* mixing) that maps the particles from their initial position $\boldsymbol{x}_0$ to their position $\boldsymbol{x}_t$ at time t. Given a PCA using

the state $\boldsymbol{x}_t$ and the initial state $\boldsymbol{x}_0$, let $\boldsymbol{\Lambda} \in \mathbb{R}^{d \times d}$ be the resulting diagonal matrix of the eigenvalues, λ_j the eigenvalues and $\boldsymbol{R}$ the corresponding matrix of eigenvectors with $\boldsymbol{r_j}$ the column eigenvector associated with λ_j. A major assumption in PCA is that linearity frames the problem [40]. Consequently, if the largest eigenvalue $\lambda_k = \max(\lambda_j)$ tends toward a constant value, a direction $\boldsymbol{r}_k$ exists that explains a larger portion of the variance than any other direction. If this value is large, the system is considered ill-mixed because an axis obtained after a linear change of basis represents f. However, if f is a non-linear function, then λ_k can decrease asymptotically to zero even if this transformation does not lead to efficient mixing. In fact, an uncountable amount of functions exist that lead to a vanishing mixing index, but that do not actually lead to efficient mixing. Therefore, an asymptotically vanishing mixing index is a necessary, but not a sufficient condition for a well-mixed system. That is, if the mixing index decreases toward a non-vanishing large constant then the system is poorly mixed. However, if the mixing index decreases toward zero, the system may or may not be mixed. This critical issue was not discussed in [28] and will now be illustrated using a simple, yet realistic, example.

Consider a circle filled with particles in the configuration depicted in Figure 1a in a 2D ($x - y$ or $r - \theta$) plane. Initially, the particles are segregated by their

color in the θ and r directions. A time-independent Lamb-like vortex is then applied [41] for which the velocity field $\boldsymbol{u}$ on domain $\Gamma = [-1, 1] \times [-1, 1]$ is given by:

$$\boldsymbol{u} = [u_r, \ \ u_\theta]^T \tag{9}$$

$$\boldsymbol{u} = [0, \ \ \frac{1}{5r}\left(1 - e^{-r^2}\right)]^T \tag{10}$$

where u_r and u_θ are the radial and azimuthal velocities. Figures 1b and 1c present the configuration of the particles after 200 s and 1000 s of flow. We can see that the cyan-blue and the red-yellow particles are well mixed, but that, since there is no radial flow, the system remains segregated in the r direction. Clearly this system is poorly mixed. This is no surprise, since any $2D$ stationary flow is incapable of achieving a mixed state [38].

We then study this system using the mixing index in the weak sense for long periods of time using Cartesian coordinates $\boldsymbol{x} = [x, y]^T$. The graphs in Figure 2 present the evolution of the mixing index and the associated eigenvector as annotations. We can see that, while this flow is incapable of mixing the particles in the radial direction, the mixing index decreases to a value close to zero (0.029). This is because the Lamb-like vortex is a non-linear process that mixes only in the θ direction, which violates one of the prerequisites for such analysis, *i.e.*,

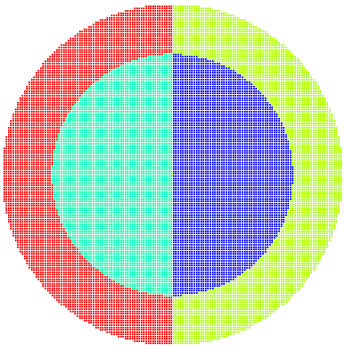

(a) Initial configuration

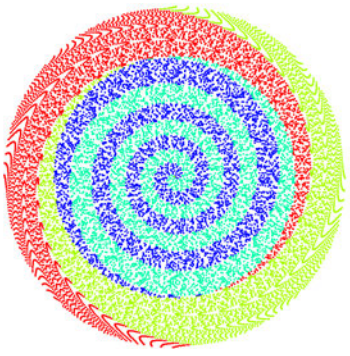

(b) Configuration after 200 s of mixing

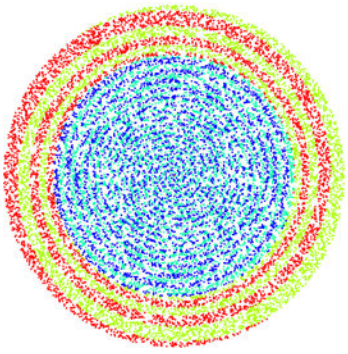

(c) Configuration after 1000 s of mixing

Figure 1: Mixing using a Lamb-like vortex

linearity.

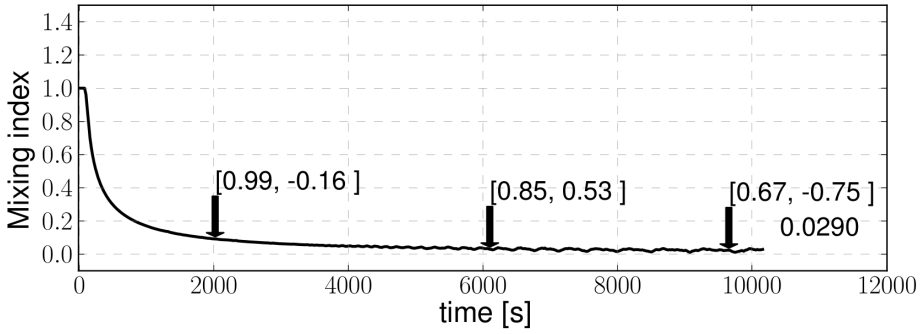

Figure 2: Evolution of the mixing index for a PCA analysis carried out in a $x - y$ coordinate system. The values in the brackets represent the eigenvectors associated with the current value of the mixing index. The last value is the final value.

One way to make the mixing index more robust is to study the system in a set of coordinates that naturally describes the corresponding process. For instance, the motion in stirred tanks is well described using cylindrical coordinates (r, θ, z). If we perform the mixing index analysis using cylindrical coordinates, we obtain the results in Figure 3 showing that the mixing index remains 1, with the associated eigenvector being $\boldsymbol{r}$. Thus, with the appropriate set of coordinates, the mixing index can identify such an ill-mixed system. From this analysis, we can conclude that while a decreasing mixing index is a necessary but not sufficient condition for a well-mixed system, its performance can be aug-

mented using an appropriate set of coordinates that more adequately describes the position of the particles. Furthermore, when the mixing index converges to a constant, non-zero value, it is an indicator of an ill-mixed system. As such, we performed all the mixing index calculations discussed in the subsequent sections using cylindrical coordinates.

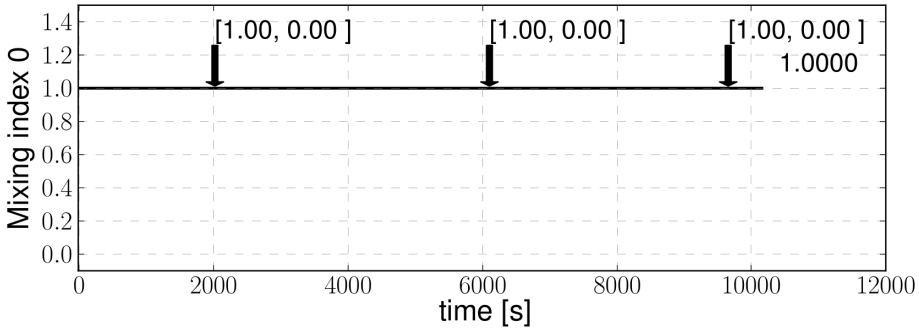

Figure 3: Evolution of the mixing index for a PCA analysis carried out in a $r - \theta$ coordinate system. The values in the brackets represent the eigenvectors associated with the current value of the mixing index. The last value is the final value.

3.2. Measuring the fraction of suspended solids

3.2.1. Pressure gauge technique

The PGT measures the fraction of suspended particles by the increase in the apparent density of a suspension due to the presence of the particles.

At the start of a mixing operation, before the impeller is put in motion, the

particles are at rest at the bottom of the tank and their weight is thus held by the lateral and bottom walls of the vessel. As the speed of the impeller is increased and the particles are progressively suspended, their weight gets held more and more by the fluid flow (*e.g.*, by the drag force) and, consequently, the apparent density of the fluid increases. This increase in density translates into an increase in hydrostatic pressure, which can be measured at the bottom of the tank. Once all the particles are suspended, the apparent density of the suspension reaches a constant value, as does the increase in static pressure (ΔP_{susp}). However, changes in the impeller velocity also induce a change in the hydrodynamic pressure, which needs to be taken into account. By fitting a parabola to the pressures obtained once all the particles are suspended, the dynamic pressure effect can be subtracted from the total pressure to isolate the changes in static pressure and, to deduce the fraction of suspended particles. This is illustrated in Figure 4. This method, which is called the pressure gauge technique (PGT) [42, 43], can be used experimentally to obtain the fraction of suspended particles. We recently showed [16, 44] that this technique can be used in a CFD-DEM model by averaging the pressure at the bottom of the tank and by applying the same procedure to correct for the dynamic pressure. The results obtained with this method for the fraction of suspended particles

compared very well with the experimental data for the laminar, transitional and turbulent regimes. However, this method can only be applied to flat-bottomed and conical vessels, and requires simulations over a large range of impeller speeds to capture the region where the dynamic pressure correction can be established. This makes it computationally intensive.

3.2.2. Lagrangian suspended fraction analysis

The Lagrangian suspended fraction analysis (LSFA) recently introduced by our group [44] can be used to calculate the fraction of suspended particles from the positions of the particles. This method is intuitively linked to the original definition of N_{js} introduced by Zwietering that states that N_{js} is the impeller speed at which no particle remains motionless at the bottom of the tank for more than 1 or 2 s. In the LSFA technique, the displacement of each particle located in a region close to the bottom of the tank is monitored during a time interval Δt_{js}. If a particle displaces by an amount larger than Δx_{js} during this interval, it is considered suspended. We investigated two different criteria based on the displacement in the axial direction (LSFA-Δz) or the overall displacement (LSFA-$\Delta \boldsymbol{x}$) and found that much better agreement was obtained between the LSFA-$\Delta \boldsymbol{x}$ and the PGT (both numerical and experimental) results for the

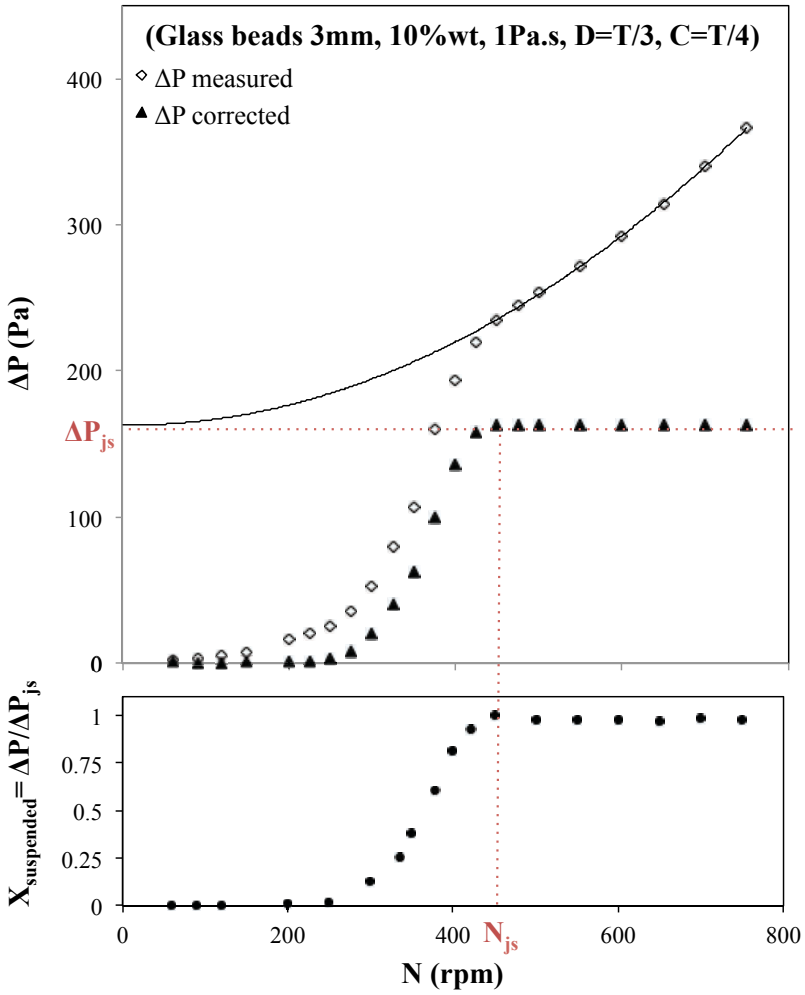

Figure 4: Evolution of the total pressure and static pressure using the pressure gauge technique. The parabola is the correction for the hydrodynamic pressure. Adapted from Blais *et al.* [16]

fraction of suspended particles. Defining the threshold values of the displacement (Δx_{js}) and the observation time (Δt_{js}) remained slightly subjective. We reported [44] that there is good agreement between Zwietering's original definition and that the PGT results can be obtained by setting $\Delta t_{js} = 2$ s and $\Delta \boldsymbol{x}_{js} = d_p$. This choice was justified by the fact that d_p is the characteristic length pertaining to the motion and dynamics of the particles. The LSFA technique is valid for any geometry and can be applied directly to a single simulation without requiring the investigation of numerous impeller speeds, unlike the PGT technique. While there is a degree of subjectivity in the choice of Δt_{js} and $\Delta \boldsymbol{x}_{js}$, this method can be used in a straightforward way to compare the efficiencies of various geometries as long as the same set of parameters are used.

3.2.3. Decorrelated fraction analysis

The decorrelated fraction analysis (DFA) technique, which was also recently introduced by our group [44], uses the mixing index of Section 3.1.2 to calculate the fraction of suspended particles by measuring the degree of decorrelation occurring in a system during a time interval Δt_{js}.

At time $t_0 + \Delta t_{js}$, only a particle that is already suspended or that got suspended during this time interval can have its position decorrelated from its

position at time t_0. Otherwise, if a particle remains unsuspended, then its position is practically unchanged and is perfectly correlated with its initial position. Therefore, the value of the mixing index (λ_k, the largest eigenvalue) should be linked to the fraction of unsuspended particles. The only assumption behind this approach is that once particles are suspended, they are also dispersed. Indeed, if particles move as large clusters, a large correlation would be retained among them. It remains to be determined whether this method can be applied in the laminar and transitional regimes where the dispersion of the particles usually occurs over a relatively long time scale.

We showed in earlier work [44] that the DFA technique can be used to measure the fraction of suspended particles in a stirred tank in the turbulent regime. We reported that the observation window should be sufficiently large to allow for the full decorrelation of the system at high impeller speed. In the case of the turbulent regime, we reported that, for $\Delta t_{js} \geq 2$ s, the results for the fraction of suspended particles were less sensitive to Δt_{js}.

The mixing index analysis in the present study is based on cylindrical coordinates ($[\boldsymbol{e}_r, \boldsymbol{e}_\theta, \boldsymbol{e}_z]$), as discussed in Section 3.1.2.

Table 3: Dimensions of the mixing set-up

Symbol	**Name**	**Dimension**
T	Tank diameter	0.365m
D	Impeller diameter	$\frac{T}{3}$
H	Liquid level	T
C	Off-bottom clearance	$\frac{T}{4}$
W_i	Blade width	$\frac{D}{5}$

4. Methodology

4.1. Mixing system

The mixing rig studied consists of a 0.365 m diameter (T) flat-bottomed, cylindrical transparent vessel equipped with a T/3 diameter (D) down-pumping pitched blade turbine (PBT) rotating in the clockwise direction. The height of the liquid is set to that of the tank diameter (H=T). The particles are glass beads (10% w/w) with a Sauter ($d_{p,32}$) diameter of 3.02 mm in a glucose solution with a viscosity of 1 Pa.s. The set-up is shown in Figure 5.

The present study is separated into two parts. The aim of the first part is to characterize the mechanisms and dynamics of the suspension of the particles as well as the influence of the DEM parameters used for the simulations. We use the set-up described by Lassaigne *et al.* [3], with a clearance of $C = T/4$. The dimensions of the mixing rig for this part of the study are summarized in Table 3.

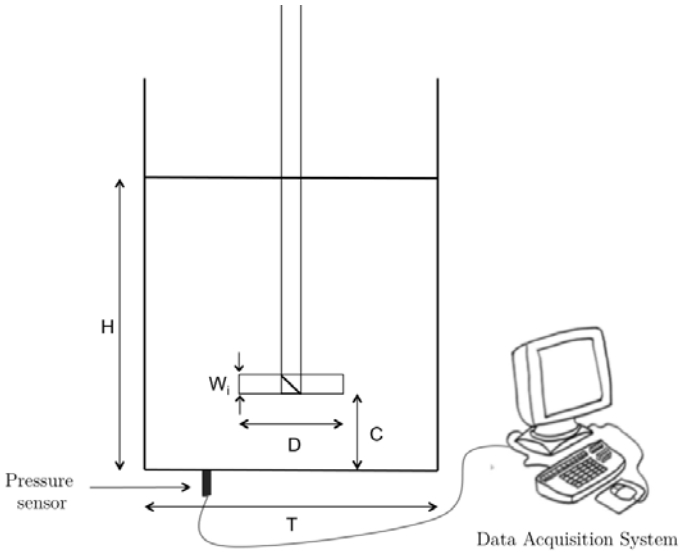

Figure 5: Experimental set-up

The aim of the second part of this work is to study the impact of the geometrical configuration (impeller clearance and presence of baffles) on the ability of the stirred tank to suspend and distribute the particles. In the present work, the clearance is set to three different standard C values ($T/5$, $T/4$, and $T/3$). The set-ups are studied with and without four baffles of width W=T/10.

4.2. Simulation set-up

The simulations were performed using the CFD-DEM model presented in Section 2. The model parameters used in the simulation are presented in Table 5. The parameters are based on the work of Di Renzo and Di Maio [45], Di

Table 4: Physical properties of the fluid and the particles

Symbol	**Name**	**Value**
ρ_f	Density of the fluid	1390 kg.m^{-3}
μ	Dynamic viscosity of the fluid	1 Pa.s
ρ_p	Density of the solid particles	2500 kg.m^{-3}
d_p	Range of particle diameters	2.66-3.5 mm
$d_{p,32}$	Sauter diameter	3.02 mm
x_s	Mass fraction of solid	10 %
ϵ_s	Volume fraction of solid	5.8 %

Renzo *et al.* [46], and Shao *et al.* [47] for glass beads suspended in a liquid. The same mechanical properties were given to both the walls and the particles. The sensitivity of the model to variations of the DEM parameters (E, e_r, μ_f) is discussed in Section 5.5. To reproduce the size distribution of the particles that was measured experimentally, 10 different diameters were used. A total of 148 700 particles were required to reproduce the mass fraction of 10%. The model used for the simulations includes all the hydrodynamic forces presented in Section 2.3. The Saffman lift force is included in this model, but was not in a previous investigation [16]. The impact of this force will be assessed in Section 5.1 by comparing the results obtained in the present study with those from the earlier investigation [16].

In the simulations, the pressure was monitored at the bottom of the tank and was averaged using the procedure described in [16].

Table 5: Parameters for the simulations of solid-liquid mixing

Symbol	**Name**	**Value**
Y	Young's modulus	100 MPa
e_r	Coefficient of restitution	0.9
ν	Poisson ratio	0.25
$\mu_{s,ij}$	Coefficient of sliding friction	0.3
$\mu_{r,ij}$	Rolling friction	0.1
Δt_{DEM}	DEM time step	5×10^{-6}
Δt_{CFD}	CFD time step	1×10^{-4}
Δt_c	Coupling time-step	1×10^{-4}

The background hexahedral mesh used for the CFD consisted of 33x88x60 (r,θ,z) cells with additional mesh refinement in the swept volume of the impeller (and close to the baffles, when present), for a total of 350k (400k with the baffles) cells. We found that, for this geometry, mesh refinement past this level did not lead to any measurable change in the torque ($< 1\%$) or the velocity field [16]. The same time step was used for all the simulations. The Courant-Friedrichs-Lewy condition was satisfied for all the simulations and was below 0.75. The coupling time step Δt_c was chosen to ensure stable solid-fluid coupling as per our previous stability analysis [16]. The time step for the DEM particles was below 15% of the characteristic time of Rayleigh waves (Δt_{Ra}) ensuring the stability of the DEM part. The expression for Δt_{Ra} is:

$$\Delta t_{Ra} = \frac{\Pi}{2} d_p \sqrt{\frac{\rho_p}{G}} \left(\frac{1}{0.1631\nu + 0.8766} \right) \tag{11}$$

The dependency of the Rong drag model on the void fraction was relaxed to ensure the stability of the explicit solid-fluid and fluid-solid coupling. We refer the reader to the stability analysis performed in [16] for a thorough explanation of this procedure.

The simulations were carried out on the Briaree cluster of Compute Canada and Calcul Québec. Each simulation used 2 Intel Westmere processors, each consisting of 6 physical cores with a frequency of 2.67 GhZ and 12 Go of memory (24 Go total). All simulations were run until steady-state was reached for the pressure measured at the bottom of the tank, which led to simulation times between 100s and 200s depending on the impeller speed. The longest simulations required around 50 days of computer time each.

5. Investigation of the mixing dynamics and suspension mechanisms

In this section, we first evaluate the role of the lift force. We then investigate the dynamics of the solid-liquid mixing operation and evaluate the fraction of suspended particles and the efficiency of the mixing using the approaches presented in Section 3, namely the LSFA-$\Delta \boldsymbol{x}$, DFA, and mixing index techniques. We then investigate the role of the particle properties in order to establish the sensitivity of the model to the DEM parameters and to isolate the dominant

particle-particle forces.

5.1. Validation of the model with lift forces

We recently studied the mixing system considered in this work without including the Saffman lift force for the solid-fluid interactions [16]. However, given the high viscosity of the suspension and the high shear forces at the surface of the bed of particles, these forces could potentially influence the fraction of suspended particles when in a partially suspended state.

The graph in Figure 6 presents the evolution of the fraction of suspended particles as a function of the impeller speed, as measured by the PGT, with and without the Saffman lift force, and compares it to the experimental data of Lassaigne *et al.* [3].

It can be seen that adding the Saffman lift force increases the fraction of suspended particles slightly for all impeller speeds, but does not affect the results significantly. In both cases (with and without the lift forces), the model appears to slightly overestimate the fraction of suspended particles for $N < 400$ RPM . The impeller speed $N = 425$ RPM corresponds to N_{js} since, according to the experimental and numerical PGT results, all the particles are suspended.

We conclude from these results that the Saffman lift force plays a negligible

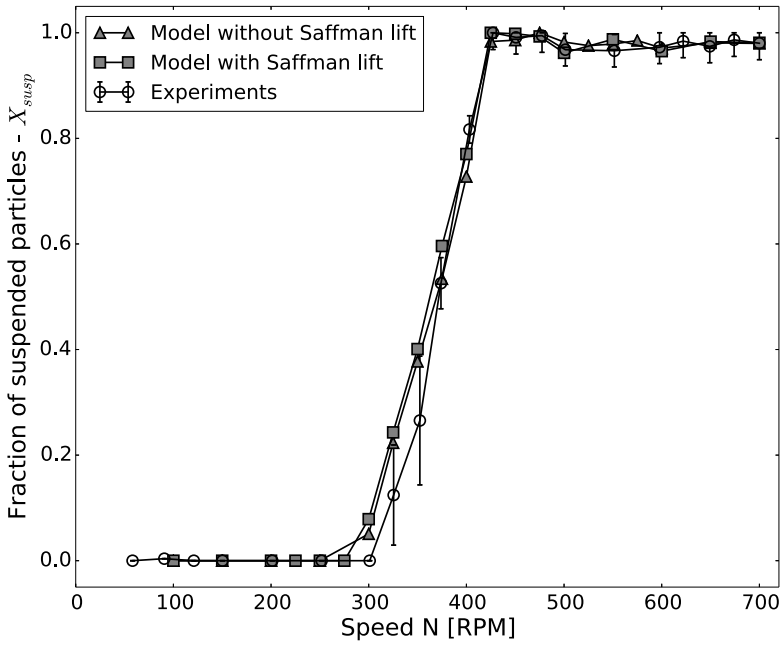

Figure 6: Evolution of the fraction of suspended particles as function of the impeller speed, as measured in the numerical simulations with and without lift forces, and in the experiments

role in the suspension of the particles.

5.2. Flow patterns and solids distribution

The velocity profiles, the particle concentration profiles and the particle dynamics are next considered. All the slices of the stirred vessel presented in this section were obtained by averaging the quantity of interest over multiple impeller rotations (at least more than 10) in the plane of the normal vector $\boldsymbol{e}_y$ ($P_{\boldsymbol{y}}$ plane).

The slices in Figure 7 present the phase-averaged solid volume fraction (or concentration) for three impeller speeds (150, 250, and 350 RPM), while Figure 8 shows the corresponding velocity profiles. Since the impeller is a down-pumping PBT, fluid is ejected from the impeller and is stopped by the initially static particle bed. Then, as can be seen, the particles are only suspended in a region below the impeller at low speed, leading to the formation of an umbrella structure below the impeller. Increasing the velocity leads to the onset of erosion where the particles ascended along the lateral walls of the tank. As soon as they are eroded along these walls, the particles are able to reach a considerable height due to the high viscosity of the fluid. The particles become increasingly distributed and dispersed as the impeller speed is increased.

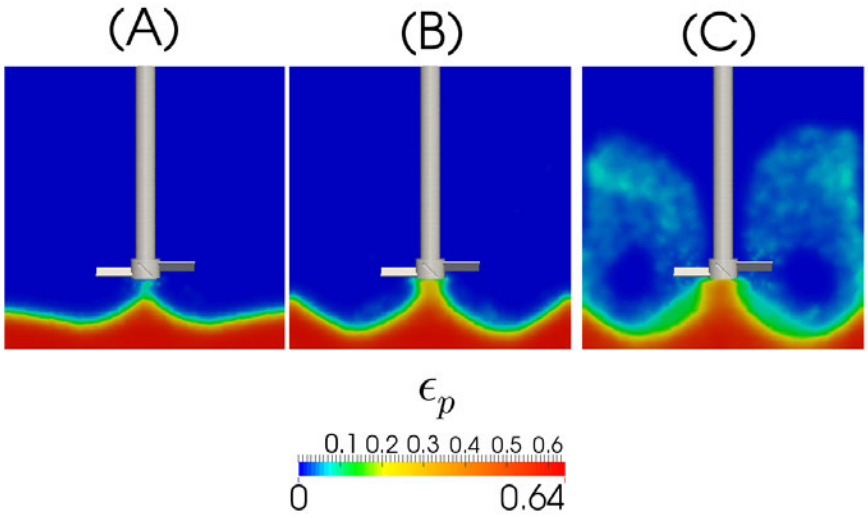

Figure 7: Phase-averaged solid volume fraction in the P_y plane for impeller speeds of (A) 150 RPM, (B) 250 RPM and (C) 350 RPM

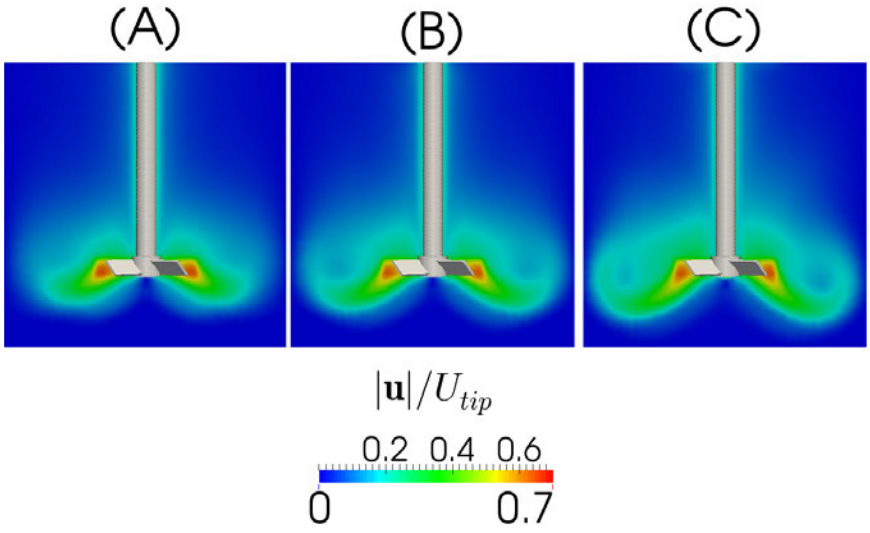

Figure 8: Phase-averaged velocity magnitude in the P_y plane for impeller speeds of (A) 150 RPM, (B) 250 RPM and (C) 350 RPM

Figures 9 and 10 show the phase-averaged solid fraction and velocity profiles for higher impeller speeds of 450, 550 and 650 RPM, respectively. As can be seen, at all these speeds, the PBT behaves much like a radial discharge impeller since the fluid jets coming out of the impeller blades are directed toward the lateral walls. For values of N larger than $N_{js} = 425$ RPM predicted by the PGT technique, a significant amount of particles accumulate in a dense conical region directly below the impeller, as can be seen in Figure 9. An examination of the pressure profiles (not shown here) revealed that the accumulation of particles appears in part to be due to the negative dynamic pressure below the impeller

caused by the high speed of the impeller rotation and the large rigid body-like, angular motion of the fluid therein. It should be noted that the size of this dense cone of particles tends to decrease slightly as the impeller speed increases from $N = 450$ to $N = 650$ RPM.

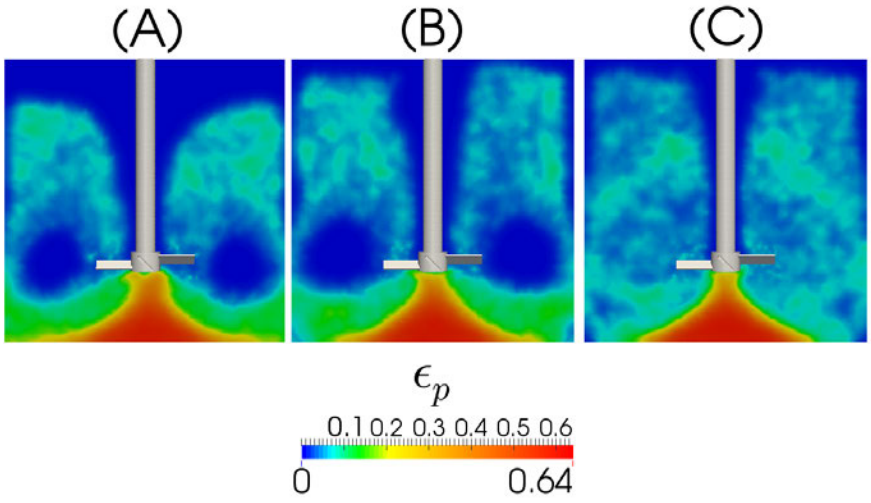

Figure 9: Phase-averaged solid fraction in the P_y plane for impeller speeds of (A) 450 RPM, (B) 550 RPM and (C) 650 RPM.

It is quite clear, however, that while the PGT technique indicates full suspension, the system does not reach a fully suspended state even at an impeller

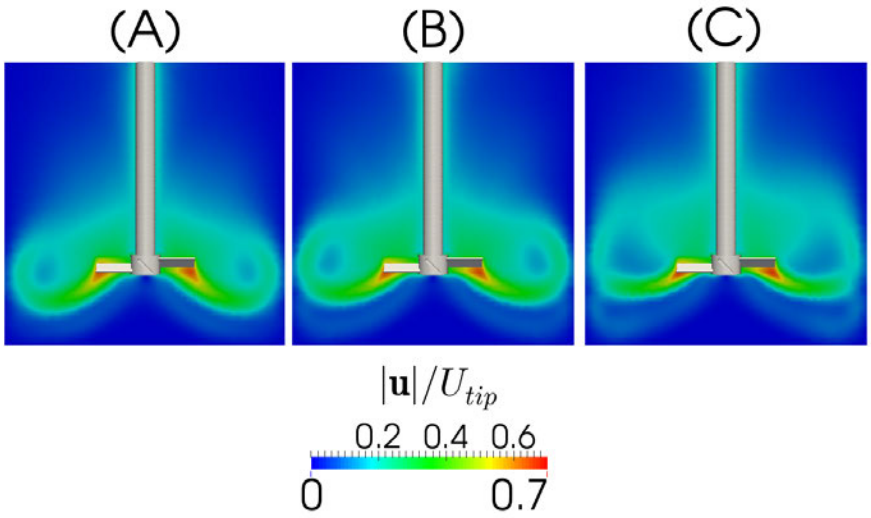

Figure 10: Phase-averaged velocity magnitude in the P_y plane for impeller speeds of (A) 450 RPM, (B) 550 RPM and (C) 650 RPM

speed of $N = 650$ RPM. In fact, the cone of particles at the bottom of the vessel is at least stable for $N \in [425, 700]$ RPM and might remain stable at higher impeller speed. Consequently, increasing the speed past $N = 425$ RPM does not significantly increase the number of suspended particles and, as a result, the hydrostatic pressure remains constant for $N > 425$ RPM. Thus, when the dynamic pressure correction is applied to the PGT, the system appears to be fully suspended at $N = 425$ RPM since the maximal value of the hydrostatic pressure is reached at this velocity. However, it must be kept in mind that approximately 5 to 10 % of the particle volume remains unsuspended or at least isolated from the bulk of the flow for $N \geq 425$ RPM.

Based on these results, it appears that the PGT technique should be used with care. It only provides a valid assessment of the fraction of suspended particles if the system is able to reach full suspension. This is not the case for the present mixing system.

Furthermore, at lower impeller speeds ($N = 450$ and 550 RPM), Figures 9 (A) and (B) reveal that toroidal zones devoid of particles appear at the top of the impeller blade. Similar zones were identified previously by Lamberto *et al.* [48] and Cabaret *et al.* [49] using colorimetric experiments with single phase flow systems and various types of impellers. We recently showed [44] that this

structure can also appear in a turbulent regime when baffles are present. At a higher impeller speed ($N \geq 650$ RPM, Figure 9 (C)), the toroid becomes unstable and disappears.

The cross-section in Figure 11 shows the logarithmic values of the particle Reynolds number ($Re_p = \frac{\rho_f d_p |\boldsymbol{u}-\boldsymbol{v}|}{\mu}$) for an impeller speed of 650 RPM. It can clearly be seen that, with the exception of the regions near the impeller and close to the lateral walls, the particle Reynolds number is very low, indicating that, in the bulk of the flow, the particles behave like a passive scalar. Since the particles follow the streamlines in the bulk of the flow, they are able to rise sufficiently high in the liquid. This explains why the particles are well distributed in the phase-averaged solid fraction profiles of Figures 9 (B) and (C).

5.3. Lagrangian analysis of the fraction of suspended solids

While the PGT predicts a fully suspended state (numerically and experimentally) based on observations of the phase-averaged volume fraction, a portion of the particles accumulate and remains unsuspended at the bottom of the vessel below the impeller, even at high impeller speeds.

We used the DFA and LSFA-$\Delta\boldsymbol{x}$ techniques to analyze the fraction of suspended particles based on their position.

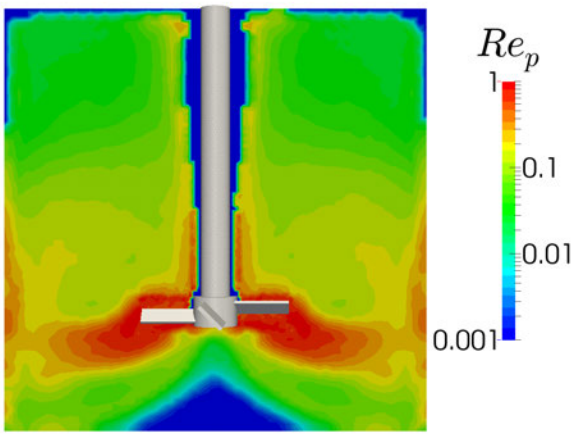

Figure 11: Phase-averaged particle Reynolds number (Re_p) in the $P_{\boldsymbol{y}}$ plane for $N = 650$ RPM. Note that the scale is logarithmic.

The graph in Figure 12 shows the fraction of suspended particles obtained with the LSFA-$\Delta\boldsymbol{x}$ technique. At low impeller speeds, LSFA-$\Delta\boldsymbol{x}$ appears to overestimate the fraction of suspended particles compared to the PGT results. This is due to the motion of the particles at the top of the particle bed, which are considered suspended by the LSFA-$\Delta\boldsymbol{x}$ technique since they are in motion, but which does not appear in the PGT measurements since their weight is still partially held by the walls of the vessel or the particles underneath them. Better agreement with the experimental measurements is obtained at higher impeller speeds. However, even at higher speeds, the fraction of suspended particles

X_{susp} measured by the LSFA-$\Delta \boldsymbol{x}$ technique reaches a maximum of $X_{susp} = 96\%$ for $\Delta x_{js} = d_p$ and $\Delta t_{js} = 2$ s when N reaches 450 RPM, before leveling off to a plateau at $X_{susp} = 91\%$ for $\Delta x_{js} = d_p$ and $\Delta t_{js} = 2$ s, indicating incomplete suspension. This result is consistent with the void fraction profiles obtained in Section 5.2 and indicates that the system is incapable of reaching a fully suspended state. However, the presence of a maximum at $N = 450$ RPM with the LSFA-$\Delta \boldsymbol{x}$ technique is surprising. This is possibly an artifact of the method where some particles are considered suspended because they are in motion, despite the fact that they are still in contact with the particles at the bottom of the vessel. This LSFA-$\Delta \boldsymbol{x}$ result is not in agreement with the phase averaged solid concentration of Figure 10 where the size of the cone appears to decrease with an increase in the impeller speed.

The graph in Figure 13 shows the decorrelated fraction as a function of the impeller speed for the DFA technique and three values of the time interval Δt_{js}. It can clearly be seen that the DFA results do not coincide with the fraction of suspended particles measured by the PGT or the LSFA-$\Delta \boldsymbol{x}$ technique in Figure 12. In a previous study [44], the DFA technique was used in the turbulent regime. Thus, as soon as the particles were suspended, they were distributed and dispersed, and were thus decorrelated. This method could thus be used to

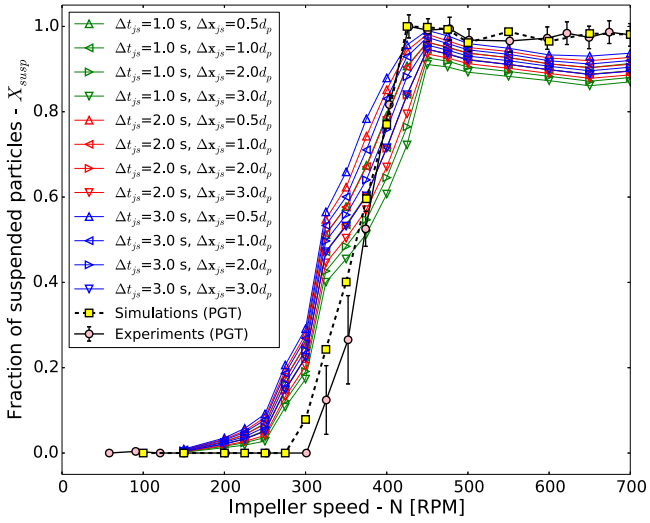

Figure 12: Evolution of the fraction of suspended particles as measured by the LSFA-$\Delta \boldsymbol{x}$ technique and comparison with the PGT results

directly assess the fraction of suspended particles in the turbulent regime. In the present case, the flow is laminar or transitional and the dispersion of the particles thus occurs over a much longer time scale ($>> \Delta t_{js}$) since there is no turbulent eddies to contribute to their motion. It thus appears that the DFA technique cannot be used with the laminar and transitional regimes to measure the fraction of suspended particles.

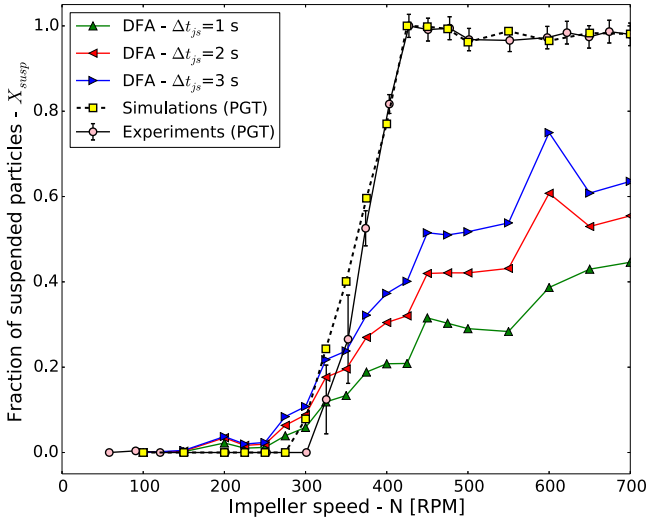

Figure 13: Evolution of the fraction of suspended particles as measured by the DFA technique and comparison with the PGT results

5.4. Mixing index

The results obtained with the solid concentration profiles and the LSFA-$\Delta \boldsymbol{x}$ technique in Sections 5.2 and 5.3, respectively, show that the system does not reach a fully mixed state since not all the particles are fully suspended. However, it remains to be determined whether the particles within the cone below the impeller circulate between the cone and the bulk of the flow or whether they remain isolated.

The mixing index is able to measure the degree of mixing and thus can be used to identify the presence of dead zones. The graph in Figure 14 displays the value of the mixing index after 100 s of mixing as a function of the impeller speed. As can be seen, the mixing index decreases before reaching a minimum value at $N = 450$ RPM and then increases asymptotically to a positive value. This is in agreement with the observed results of the LSFA-$\Delta \boldsymbol{x}$ analysis and indicates that particles not only accumulate within the cone below the impeller, but that they remain in this position indefinitely.

It is interesting to note that for all $N \geq 450$ RPM, the eigenvector corresponding to the mixing index (λ_k) is $\boldsymbol{r_k} = 0.8\boldsymbol{e}_r + 0.5\boldsymbol{e}_z$. This vector corresponds approximately to the vector normal to the cone of accumulated particles at the bottom of the tank, as can be seen in Figure 9. This once again indicates in-

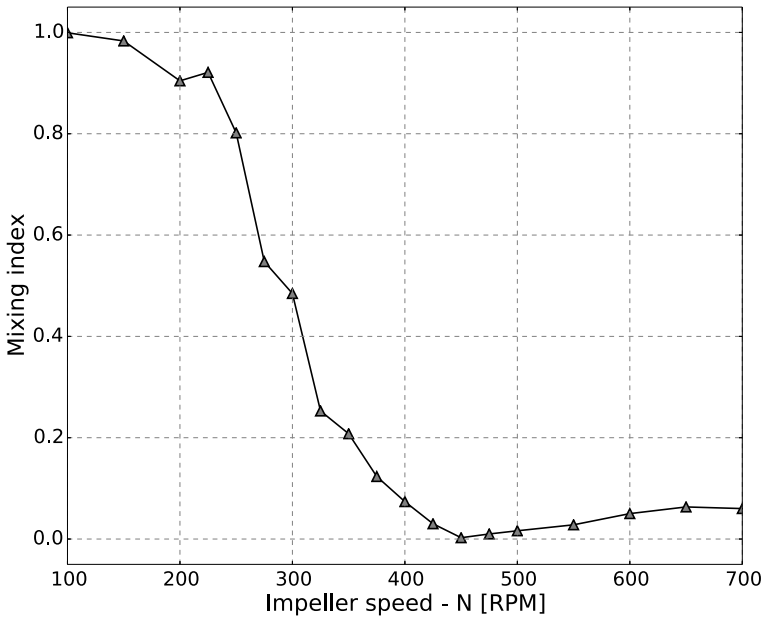

Figure 14: Evolution of the mixing index for a period of 100 s as a function of the impeller speed.

complete mixing since this direction is the one along which there is the highest degree of correlation between the particles.

5.5. Role of the mechanical properties of the particles

In a recent investigation [16], we used a set of DEM parameters taken from [45, 46, 47] for the properties of glass beads. However, in [16], we noted that the roles of the solid properties, let alone the friction coefficients (μ_s and μ_r), the coefficient of restitution (e_r) and the Young's modulus (Y), and their impact on the dynamics of solid-liquid flows were unclear. In particular, we questioned the use of a coefficient of restitution based solely on rebound experiments in air since the results reported by Gondret *et al.* [50] showed that the apparent coefficient of restitution of a particle quickly decreases towards zero when the Stokes number ($St = \frac{U\tau_p}{L}$, where τ_p is the particle relaxation time, U the fluid velocity and L a length scale) is low ($St < 1$). It is thus important to determine the sensitivity of the results obtained previously to variations of the values of these four major solid properties. The standard set-up presented in Section 4 and the solid properties considered are given in Table 6. The effect of these parameters is evaluated at four impeller speeds: $N = 250$, 375, 450 and 600 RPM. These impeller speeds correspond to four distinct regimes (see Section 5.6): the for-

Table 6: Sets of particle mechanical properties considered to assess their impact on flow dynamics

Case	μ_s	e_r	Y	μ_r
std	0.3	0.9	100 MPa	0.1
soft	0.3	0.9	**10 MPa**	0.1
hard	0.3	0.9	**1000 MPa**	0.1
inelastic	0.3	**0.01**	100 MPa	0.1
low μ_s	**0.1**	0.9	100 MPa	0.1
high μ_s	**0.9**	0.9	100 MPa	0.1
no-tf (no tangential forces)	-	0.9	100 MPa	0.1
low μ_r	0.3	0.9	100 MPa	**0.01**
high μ_r	0.3	0.9	100 MPa	**1**

mation of an umbrella of particles ($N = 250$ RPM), erosion above the impeller ($N = 375$ RPM), close to N_{js} measured via the PBT ($N = 450$ RPM), and at high impeller speeds where the particles are well distributed ($N = 600$ RPM).

The graphs in Figures 15 and 16 present the evolution of the pressure at the bottom of the tank at impeller speeds of 250, 375, 450 and 600 RPM for the cases described in Table 6. As can be seen, reducing the coefficient of restitution (*std* or *inelastic*) or changing the stiffness (*std*, *soft* or *hard*) of the particles at all velocities have no effect on the dynamics of the suspension since all pressure curves are superimposed on the *std* curve. Given the large changes applied to the stiffness and coefficient of restitution in these cases, we can conclude that the model is not sensitive to variations of these parameters and, consequently, they do not require a fine calibration.

The effect of the coefficient of sliding friction μ_s and of rolling friction μ_r is more pronounced. At a low impeller speed ($N = 250$ RPM), where the eroded particles are in the umbrella region below the impeller, changing these friction coefficients does not alter the formation of this structure (not shown here), indicating that this coherent and stable pattern is not due to friction forces or particle/particle contacts.

At $N = 375$ RPM, as can be seen in Figure 15, the friction coefficients (both μ_r and μ_s) play a significant role. Increasing one of the friction coefficients increases the fraction of suspended particles as well as the speed at which the particles are eroded. In fact, at such a speed, the PGT predicts 50% of the particles are suspended in the *std* case (Figure 6). Allowing perfect slip between the particles ($\mu_s = 0$) prevents the particles from being suspended. At an impeller speed of 450 RPM, as can be seen in Figure 16, the friction coefficients only affect the speed at which the particles are eroded, but does not affect the status of the suspension at steady state. At an impeller speed of $N = 600$ RPM, changing the value of the friction coefficients (μ_s or μ_r) does not alter the dynamics of the mixing in any fashion.

Based on the PGT measurements of Figures 15 and 16, it appears that the coefficients of friction (μ_s and μ_r) only alter the fraction of suspended particles

at intermediate impeller speeds and the time it takes for steady state to be reached. The coefficient of rolling friction μ_r appears to have a lesser impact on the fraction of suspended particles, since increasing it by a factor of 10 leads to an effect similar to that of increasing the sliding friction coefficient by a factor of 3. However, It is hard to compare the relative impact of changing the magnitude of μ_r or μ_s since these two types of friction are governed by different mechanisms and only a limited number of parameters (3 for μ_r, 4 for μ_s) were investigated. However, we can conclude from these results that μ_s and μ_r are the only DEM parameters that require calibration for this type of viscous solid-liquid flows. This is a significant finding since it implies that the other model parameters do not affect significantly the particles and flow dynamics.

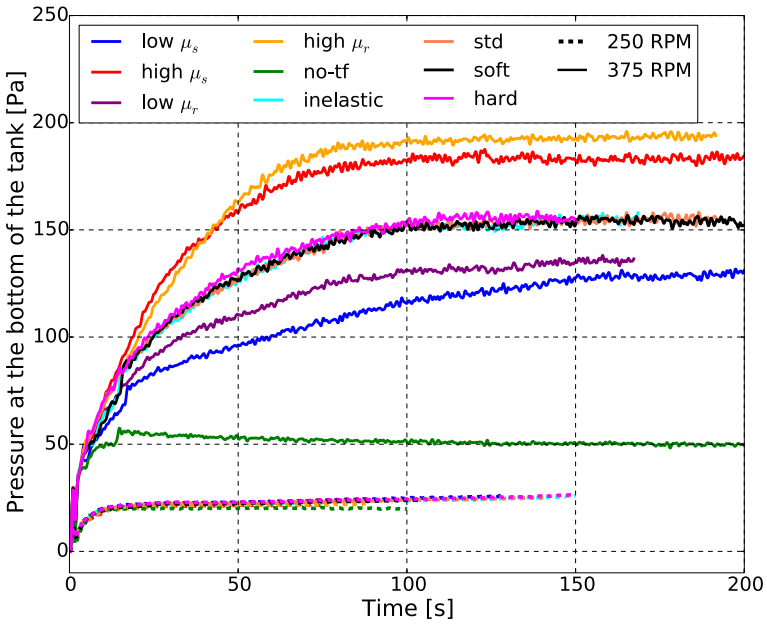

Figure 15: Influence of particle properties on the pressure measured at the bottom of the tank for $N = 250$ RPM and $N = 375$ RPM. Note the superposition of the *std*, *inelastic*, *soft* and *hard* curves for both impeller speeds.

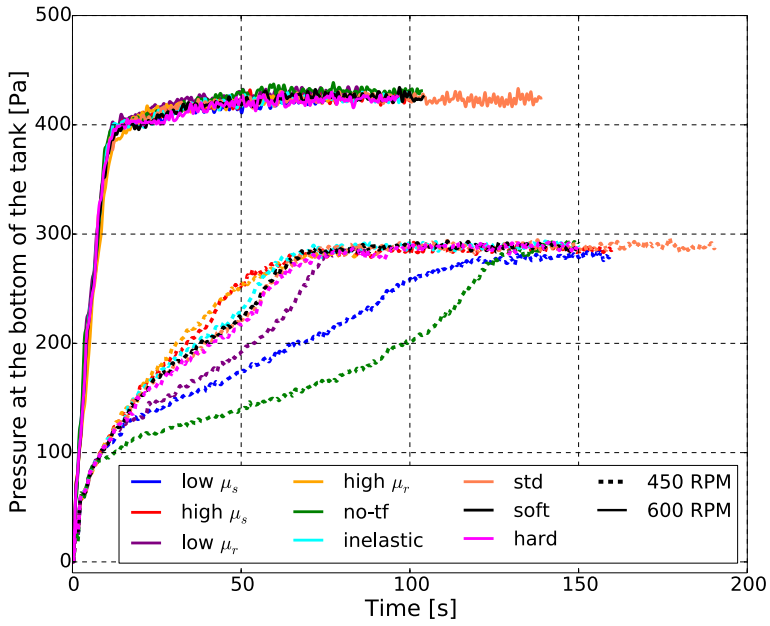

Figure 16: Influence of particle properties on the pressure measured at the bottom of the tank for $N = 450$ RPM and $N = 600$ RPM. Note the superposition of the *std*, *inelastic*, *soft* and *hard* curves for both impeller speeds.

5.6. Discussion on the suspension mechanisms

Some partial conclusions can be drawn from our analyses. First, four distinct regimes can be established for the solid-liquid dynamics that occurs in the mixing rig investigated:

- At a low impeller speed ($N < 150$ RPM), only a gentle "simmering" occurs at the top of the particle bed, but no particles are suspended.
- For $N \in [150, 275]$ RPM, the particles are drawn below the impeller and remain therein, forming an umbrella, and as such, do not circulate in the bulk of the tank.
- For $N > 275$ RPM, the umbrella of particles is still present, but the particles begin to erode and are lifted in the bulk of the flow toward the lateral walls.
- For $N > 450$ RPM, some particles remain unsuspended underneath the impeller. Increasing the impeller speed increases the maximal height reached by the particles.

We showed using flow visualization, the LSFA-$\Delta\boldsymbol{x}$ technique, and the mixing index that at all impeller speeds, a dead zone is present in the center of the

vessel below the impeller where the particles accumulate and are not allowed to circulate in the bulk of the flow. Thus, the system in this configuration cannot be fully mixed except possibly by greatly increasing the impeller speed ($N > 700$ RPM).

Our investigation of the role of the DEM parameters also highlighted the fact that the coefficient of sliding friction is the particle-particle collision property that plays the key role in the dynamics of erosion of the particles. This is in agreement with the experimental findings of Lassaigne *et al.* [3], who reported that the suspension of particles seemed to behave like the erosion of a particle bed, where the Shields number ($\theta = \frac{\tau}{(\rho_p - \rho_f) g d_p}$ where τ is the shear stress) is the key parameter. Our results indicate that particles are indeed put in motion by the shear stress linked to particle-particle collisions in the upper layer of the particle bed.

6. Influence of mixer characteristics

Lastly, we investigated in this section the influence of the bottom clearance (C) and the presence of baffles, on the solid-liquid dynamics, the fraction of suspended particles and their distribution in the tank.

We consider three clearances ($C = \frac{T}{5}$, $\frac{T}{4}$ and $\frac{T}{3}$), with and without baffles.

The case where $C = \frac{T}{4}$ and without baffles corresponds to the set-up studied in Section 5.

The graph in Figure 17 shows the evolution of the fraction of suspended particles measured using the LSFA-$\Delta\boldsymbol{x}$ technique with $\Delta x_{js} = d_p$ and $\Delta t_{js} =$ 2s, for all six cases investigated.

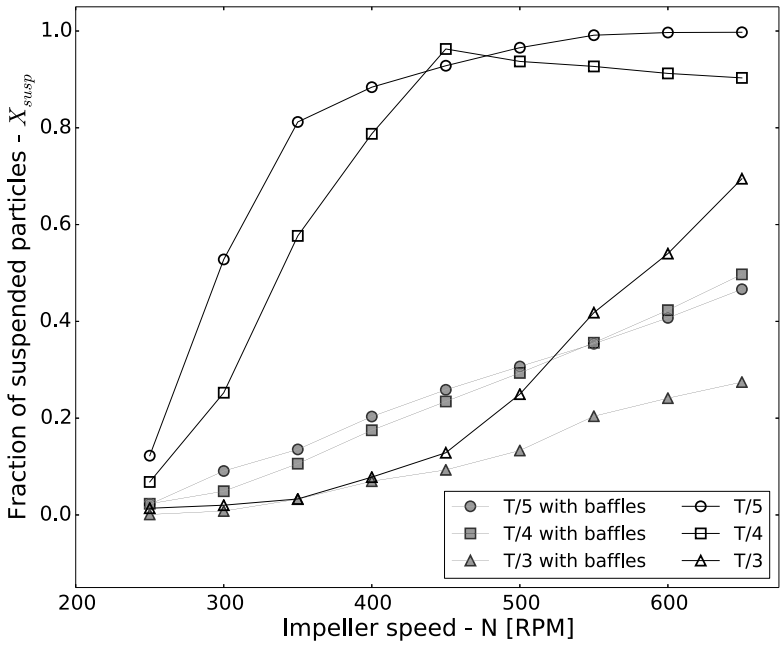

Figure 17: Fraction of suspended solids as a function of impeller speed for the six configurations investigated

It can be seen that the baffled configurations are unable to suspend the par-

ticles at the impeller speeds investigated. They perform very poorly compared to the unbaffled configurations. The velocity profiles (not shown here) show that the baffles greatly inhibit the axial flow produced by the PBT. This prevents the erosion of the particle bed and greatly reduces the height reached by the suspended particles. In fact, of baffles amplify the radial discharge when the PBT is operated in the laminar or transitional regime.

As can be seen in Figure 17, increasing the clearance from $T/4$ to $T/3$ is detrimental to the suspension of the particles. As revealed by the solid fraction profiles in Figure 18, a cone of particles similar to the cone formed at $C = T/4$ forms below the impeller. However, since the impeller is positioned significantly higher, there is a larger zone below the impeller where there is no flow and a negative pressure. This leads to the accumulation of a much larger amount of particles.

Decreasing the clearance from $C = T/4$ to $C = T/5$ increases the fraction of suspended particles at all impeller speeds, with perhaps an exception at $N = 450$ RPM, for which X_{susp} is slightly higher for $C = T/4$. Figure 19 shows the void fraction for the two clearances at $N = 450$ RPM. The accumulated particles are close to the bottom-vessel junction whereas most of the unsuspended particles for the $C = T/4$ case are below the impeller.

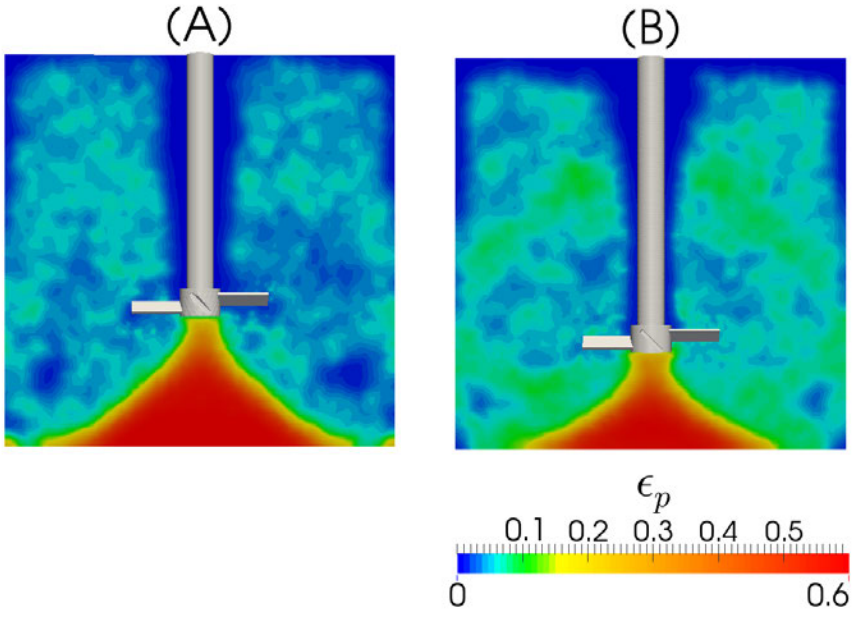

Figure 18: Solid volume fraction ($\epsilon_p = 1 - \epsilon_f$) on the $P_{\boldsymbol{y}}$ cross-section at $N = 650$ RPM for (A) $C = T/3$ and (B) $C = T/4$

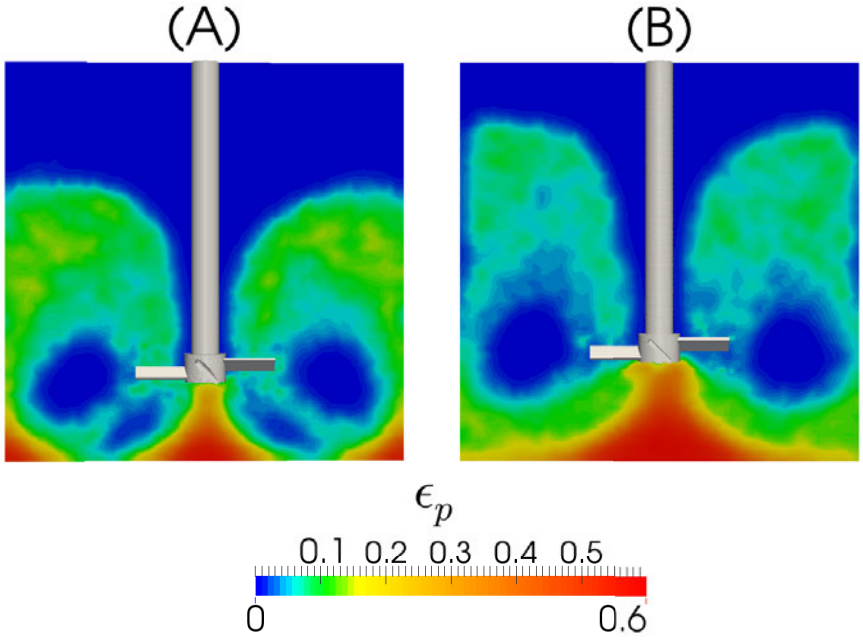

Figure 19: Solid volume fraction ($\epsilon_p = 1 - \epsilon_f$) on the $P_{\boldsymbol{y}}$ cross-section at $N = 450$ RPM for (A) $C = T/5$ and (B) $C = T/4$

At an impeller speed of $N = 650$ RPM, the $C = T/5$ configuration is able to fully suspend almost all the particles, as can be seen in Figures 17 and 20, whereas the fraction of suspended particle in the $C = T/4$ configuration does not approach unity as the particles accumulate in the cone below the impeller. This is because the cone barely existed for $C = T/5$. At such a low clearance, the structure is not stable since the hydrodynamic interactions between the impeller and the bottom of the tank are much more significant.

The cross-sections in Figure 19 show that the eroded particles reach a greater height for $C = T/4$ than for $C = T/5$, indicating that using a lower clearance slightly inhibits the distribution of the particles throughout the tank. However, even for the lowest clearance, the particles are able to reach the top of the vessel at higher impeller speeds, as can be seen in Figure 20.

Figures 19 and 20 show that toroidal zones that are depleted of particles are present for both impeller clerances. For $C = T/4$, this zone is slightly above the impeller blades whereas there are two zones for $C = T/5$: a large one at the same level as the blades and a smaller one below the blades. While this structure broke down at an impeller speed of $N \geq 600$ for $C = T/4$, it remains stable at an impeller speed of $N = 650$ RPM for $C = T/5$.

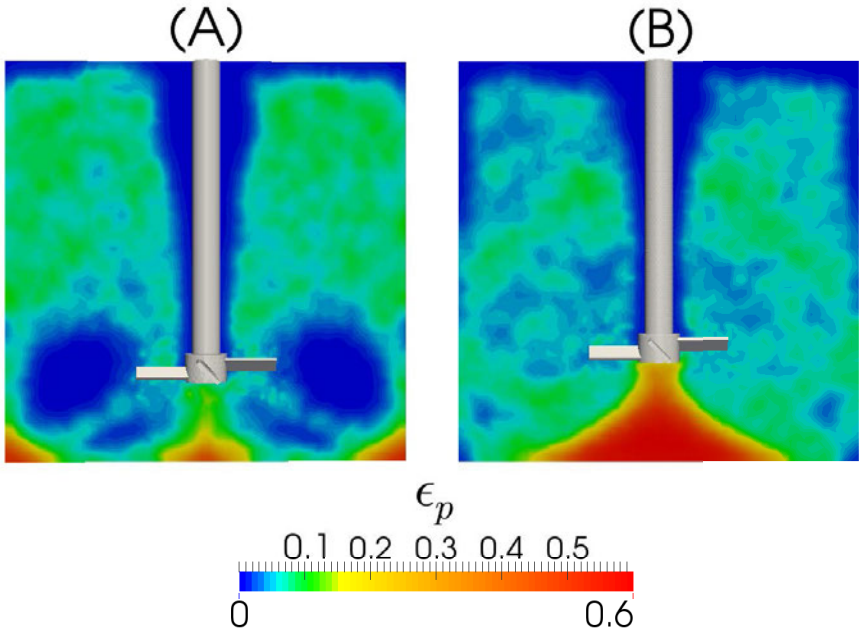

Figure 20: Solid volume fraction ($\epsilon_p = 1 - \epsilon_f$) on the $P_{\boldsymbol{y}}$ cross-section at $N = 650$ RPM for (A) $C = T/5$ and (B) $C = T/4$

7. Conclusion

The solid-liquid mixing of viscous suspensions is a challenging topic since little is known about the laminar and transitional regimes in which it occurs. We previously showed [16, 3] that a general understanding for the turbulent regime cannot be applied in a straightforward way to the laminar and transitional regimes.

In the present study, we used the unresolved CFD-DEM model previously developed by our group [16, 44], which is based on the CFDEM framework, to study solid-liquid mixing in a stirred tank (with and without baffles) equipped with a PBT at varying impeller clearances.

We first showed that the Saffman lift force does not play a significant role in the suspension dynamics. We then investigated the phase averaged solid fraction and velocity profiles, and showed that the extent of erosion of the bed of particles depends on the impeller speed. The flow patterns indicated that the PBT mainly behaves like a radial discharge impeller in the laminar and transitional regimes. It was only at higher impeller speeds that the particles become suspended along the lateral walls and reach the bulk of the flow.

However, full suspension was never achieved as some particles accumulated

in a static conical region below the impeller. We used the LSFA-$\Delta \boldsymbol{x}$ technique and the mixing index to show that these particles never get suspended and are not put significantly into motion, indicating that this cone is, in reality, a dead zone.

The sensitivity of the model to the DEM parameters was investigated. It was shown that amongst the four main DEM parameters (Young's modulus Y, coefficient of restitution e_r, sliding and rolling friction coefficients, μ_s and μ_r), only the two friction coefficients had an impact on the mixing dynamics. Indeed, changing the value of these coefficients modified the fraction of suspended particles for velocities at which partial suspension was observed, and affected the time it took to reach a steady suspended fraction of particles.

We investigated alternative geometrical configurations by varying the clearance and by adding baffles, and found that the addition of baffles greatly inhibits the axial component of the flow and prevents the suspension of particles. Increasing the clearance was detrimental to the suspension of particles and led to the formation of an even larger cone below the impeller. However, decreasing the clearance to $C = T/5$ allowed for the full suspension of the particles, at an impeller speed of 600RPM and, overall, proved to be more efficient at suspending the particles than the $C = T/4$ clearance at all impeller speeds. The only

exception is perhaps at $N = 450$ RPM where the behavior was slightly better with $C = T/4$. In particular, the cloud height reached by the particles was lower at $C = T/5$ than for $C = T/4$.

Consequently, it appears that better suspension can be achieved by decreasing the clearance when using a PBT in the laminar regime. Increasing the impeller diameter, which was not investigated in the present work, would most likely lead to the formation of an even bigger cone of particles and a larger dead zone.

Our work showed that the unresolved CFD-DEM model developed by our group can be used to help in the design of solid-liquid mixing operations and in the choice of an optimal geometry in order to enhance not only the fraction of suspended particles, but also the flow patterns and particle distribution. Future investigation should examine other geometries, including close-clearance impellers in the laminar regime as well as more traditional radial, mixed and axial discharge impellers in the turbulent regime using the LES extension of this model, which was introduced by our group in a previous publication [44].

8. Acknowledgements

The financial support from the Natural Sciences and Engineering Research Council of Canada (NSERC) is gratefully acknowledged. In particular, Bruno Blais is thankful for the NSERC Vanier Scholarship. Computations were made on the supercomputer Briaree from the University of Montreal, managed by Calcul Québec and Compute Canada. The operation of this supercomputer is funded by the Canada Foundation for Innovation (CFI), Ministère de l'Économie, de l'Innovation et des Exportations du Québec (MEIE), RMGA and the Fonds de recherche du Québec - Nature et technologies (FRQ-NT). The authors would like to highlight the support received from Calcul Québec analysts.

References

[1] F. Kneule, Die prüfung von rührern durch löslichkeitsbestimmung, Chemie Ingenieur Technik 28 (3) (1956) 221–225.

[2] T. N. Zwietering, Suspending of solid particles in liquid by agitators, Chemical Engineering Science 8 (3) (1958) 244–253.

[3] M. Lassaigne, B. Blais, L. Fradette, F. Bertrand, Experimental investigation of the mixing of viscous liquids and non-dilute concentrations of

particles in stirred tanks, Submitted to Chemical Engineering Research & Design (2015) .

[4] S. B. Ibrahim, A. W. Nienow, The effect of viscosity on mixing pattern and solid suspension in stirred vessels, Eighth European Conference on Mixing (136) (1994) 25–32.

[5] S. Ibrahim, A. W. Nienow, Comparing impeller performance for solid-suspension in the transitional flow regime with Newtonian fluids, Chemical Engineering Research and Design 77 (8) (1999) 721–727.

[6] A. W. Nienow, Suspension of solid particles in turbine agitated baffled vessels, Chemical Engineering Science 23 (12) (1968) 1453–1459.

[7] G. Baldi, R. Conti, E. Alaria, Complete suspension of particles in mechanically agitated vessels, Chemical Engineering Science 33 (1) (1978) 21–25.

[8] K. Raghava Rao, V. Rewatkar, J. Joshi, Critical impeller speed for solid suspension in mechanically agitated contactors, AIChE journal 34 (8) (1988) 1332–1340.

[9] K. Takahashi, H. Fujita, T. Yokota, Effect of size of spherical particle on

complete suspension speed in agitated vessels of different scale., Journal of chemical engineering of Japan 26 (1) (1993) 98–100.

[10] P. M. Armenante, E. U. Nagamine, Effect of low off-bottom impeller clearance on the minimum agitation speed for complete suspension of solids in stirred tanks, Chemical Engineering Science 53 (9) (1998) 1757–1775.

[11] R. Grenville, A. Mak, D. Brown, Suspension of solid particles in vessels agitated by axial flow impellers, Chemical Engineering Research and Design (2015) .

[12] A. Tamburini, A. Brucato, A. Busciglio, A. Cipollina, F. Grisafi, G. Micale, F. Scargiali, G. Vella, Solid–liquid suspensions in top-covered unbaffled vessels: Influence of particle size, liquid viscosity, impeller size, and clearance, Industrial & Engineering Chemistry Research 53 (23) (2014) 9587–9599.

[13] G. R. Kasat, A. B. Pandit, Review on mixing characteristics in solid-liquid and solid-liquid-gas reactor vessels, Canadian Journal of Chemical Engineering 83 (4) (2005) 618–643.

[14] A. Tamburini, A. Cipollina, G. Micale, A. Brucato, Particle distribution in dilute solid liquid unbaffled tanks via a novel laser sheet and image analysis based technique, Chemical Engineering Science 87 (2013) 341–358.

[15] K. Bittorf, S. Kresta, Prediction of cloud height for solid suspensions in stirred tanks, Chemical Engineering Research and Design 81 (5) (2003) 568–577.

[16] B. Blais, M. Lassaigne, C. Goniva, L. Fradette, F. Bertrand, Development of an unresolved CFD–DEM model for the flow of viscous suspensions and its application to solid–liquid mixing, Journal of Computational Physics 318 (2016) 201–221.

[17] CFDEM, CFDEM- Open Source CFD, DEM and CFD-DEM, URL : http://www.cfdem.com, 2015.

[18] C. Goniva, C. Kloss, N. G. Deen, J. A. M. Kuipers, S. Pirker, Influence of rolling friction on single spout fluidized bed simulation, Particuology 10 (5) (2012) 582–591.

[19] OpenCFD, OpenFOAM - The Open Source CFD Toolbox, URL : http://www.openfoam.com, 2014.

[20] LIGGGHTS, LAMMPS Improved for General Granular and Granular Heat Transfer Simulations, URL : hhtp://www.liggghts.com, 2015.

[21] C. Kloss, C. Goniva, LIGGGHTS Open Source Discrete Element Simula-

tions of Granular Materials Based on Lammps, John Wiley & Sons, Inc., 2011, pp. 781–788, (TMS).

[22] B. Blais, F. Bertrand, On the use of the method of manufactured solutions for the verification of CFD codes for the volume-averaged Navier–Stokes equations, Computers & Fluids 114 (2015) 121–129.

[23] L. Eça, M. Hoekstra, A. Hay, D. Pelletier, A manufactured solution for a two-dimensional steady wall-bounded incompressible turbulent flow, International Journal of Computational Fluid Dynamics 21 (3-4) (2007) 175–188.

[24] L. Eça, M. Hoekstra, A. Hay, D. Pelletier, On the construction of manufactured solutions for one and two-equation eddy-viscosity models, International Journal for Numerical Methods in Fluids 54 (2) (2007) 119–154.

[25] L. Eça, M. Hoekstra, A. Hay, D. Pelletier, Verification of rans solvers with manufactured solutions, Engineering with Computers 23 (4) (2007) 253–270.

[26] W. Oberkampf, C. Roy, Verification and Validation in Scientific Computing, Cambridge University Press, 2010.

[27] B. Blais, M. Lassaigne, C. Goniva, L. Fradette, F. Bertrand, A semi-implicit immersed boundary method and its application to viscous mixing, Computers & Chemical Engineering 85 (2016) 136–146.

[28] J. Doucet, F. Bertrand, J. Chaouki, A measure of mixing from lagrangian tracking and its application to granular and fluid flow systems, Chemical Engineering Research and Design 86 (12) (2008) 1313–1321.

[29] H. P. Zhu, Z. Y. Zhou, R. Y. Yang, A. B. Yu, Discrete particle simulation of particulate systems: Theoretical developments, Chemical Engineering Science 62 (13) (2007) 3378–3396.

[30] F. Bertrand, L. A. Leclaire, G. Levecque, DEM-based models for the mixing of granular materials, Chemical Engineering Science 60 (8-9) (2005) 2517–2531.

[31] Y. Tsuji, T. Tanaka, T. Ishida, Lagrangian numerical-simulation of plug flow of cohesionless particles in a horizontal pipe, Powder Technology 71 (3) (1992) 239–250.

[32] R. D. Mindlin, H. Deresiewica, Elastic spheres in contact under varying oblique forces, Journal of applied mechanics 20.

[33] R. Mindlin, Compliance of elastic bodies in contact, J. of Appl. Mech. 16.

[34] D. Gidaspow, Multiphase Flow and Fluidization: Continuum and Kinetic Theory Descriptions, Academic press, 1994.

[35] R. I. Issa, Solution of the implicitly discretised fluid flow equations by operator-splitting, Journal of Computational Physics 62 (1) (1986) 40–65.

[36] L. W. Rong, K. J. Dong, A. B. Yu, Lattice-Boltzmann simulation of fluid flow through packed beds of uniform spheres: Effect of porosity, Chemical Engineering Science 99 (2013) 44–58.

[37] J. B. McLaughlin, Inertial migration of a small sphere in linear shear flows, Journal of Fluid Mechanics 224 (1991) 261–274.

[38] J. M. Ottino, The kinematics of mixing: stretching, chaos, and transport, Vol. 3, Cambridge university press, 1989.

[39] J. Bouffard, F. Bertrand, J. Chaouki, H. Dumont, Discrete element investigation of flow patterns and segregation in a spheronizer, Computers & Chemical Engineering 49 (2013) 170–182.

[40] J. Shlens, A tutorial on principal component analysis, arXiv preprint arXiv:1404.1100.

[41] H. Lamb, Hydrodynamics, Cambridge university press, 1932.

[42] A. Brucato, G. Micale, L. Rizzuti, Determination of the amount of unsuspended solid particles inside stirred tanks by means of pressure measurements, Récent Progrès Génie des Procédés 11 (1997) 3–10.

[43] G. Micale, F. Grisafi, A. Brucato, Assessment of particle suspension conditions in stirred vessels by means of pressure gauge technique, Chemical Engineering Research and Design 80 (8) (2002) 893–902.

[44] B. Blais, O. Bertrand, L. Fradette, F. Bertrand, Unresolved cfd-dem simulations of non-dilute solid-liquid mixing in the turbulent regime: Prediction of suspension curve and just-suspended speed, Submitted to AIChE journal.

[45] A. Di Renzo, F. P. Di Maio, Homogeneous and bubbling fluidization regimes in DEM-CFD simulations: Hydrodynamic stability of gas and liquid fluidized beds, Chemical Engineering Science 62 (1-2) (2007) 116–130.

[46] A. Di Renzo, F. Cello, F. P. Di Maio, Simulation of the layer inversion phenomenon in binary liquid-fluidized beds by DEM-CFD with a drag law for polydisperse systems, Chemical Engineering Science 66 (13) (2011) 2945–2958.

[47] T. Shao, Y. Hu, W. Wang, Y. Jin, Y. Cheng, Simulation of solid suspension in a stirred tank using CFD-DEM coupled approach, Chinese Journal of Chemical Engineering 21 (10) (2013) 1069–1081.

[48] D. Lamberto, M. Alvarez, F. Muzzio, Experimental and computational investigation of the laminar flow structure in a stirred tank, Chemical Engineering Science 54 (7) (1999) 919–942.

[49] F. Cabaret, L. Fradette, P. A. Tanguy, New turbine impellers for viscous mixing, Chemical Engineering & Technology 31 (12) (2008) 1806–1815.

[50] P. Gondret, E. Hallouin, M. Lance, L. Petit, Experiments on the motion of a solid sphere toward a wall: From viscous dissipation to elastohydrodynamic bouncing, Physics of Fluids 11 (9) (1999) 2803–2805.